

VPHO: Joint Visual-Physical Cue Learning and Aggregation for Hand-Object Pose Estimation

Jun Zhou^{1,2,3,4}, Chi Xu^{1,2,3*}, Kaifeng Tang^{1,2,3}, Yuting Ge^{1,2,3}, Tingrui Guo^{1,2,3}, Li Cheng⁴

¹School of Automation, China University of Geosciences, Wuhan 430074, China,

²Hubei Key Laboratory of Advanced Control and Intelligent Automation for Complex Systems, Wuhan 430074, China,

³Engineering Research Center of Intelligent Technology for Geo-Exploration, Ministry of Education, Wuhan 430074, China,

⁴Department of Electrical and Computer Engineering, University of Alberta, Edmonton, AB T6G 2R3, Canada

{jchow, xuchi, tkf, gyting, guotongrui}@cug.edu.cn, lcheng5@ualberta.ca

Abstract

Estimating the 3D poses of hands and objects from a single RGB image is a fundamental yet challenging problem, with broad applications in augmented reality and human-computer interaction. Existing methods largely rely on visual cues alone, often producing results that violate physical constraints such as interpenetration or non-contact. Recent efforts to incorporate physics reasoning typically depend on post-optimization or non-differentiable physics engines, which compromise visual consistency and end-to-end trainability. To overcome these limitations, we propose a novel framework that jointly integrates visual and physical cues for hand-object pose estimation. This integration is achieved through two key ideas: 1) joint visual-physical cue learning: The model is trained to extract 2D visual cues and 3D physical cues, thereby enabling more comprehensive representation learning for hand-object interactions; 2) candidate pose aggregation: A novel refinement process that aggregates multiple diffusion-generated candidate poses by leveraging both visual and physical predictions, yielding a final estimate that is visually consistent and physically plausible. Extensive experiments demonstrate that our method significantly outperforms existing state-of-the-art approaches in both pose accuracy and physical plausibility.

Code — <https://github.com/zhoujun-7/VPHO>

Introduction

Hand-object pose estimation from single RGB images (Hasson et al. 2019) has broad applications across various fields, including virtual and augmented reality (Mueller et al. 2019; Chen et al. 2019), human-computer interaction (Ren and Bao 2020), and robotics (Billard and Kräig 2019). Most existing methods (Hampali et al. 2022; Liu et al. 2021; Lin et al. 2023; Wang, Mao, and Li 2023b) primarily rely on image-based visual cues to ensure that the 3D pose estimation is consistent with 2D observations (Zhou et al. 2024; Pavlakos et al. 2024). For example, segmentation consistency losses are widely adopted (Qi et al. 2024; Zhang et al. 2024; Xu et al. 2023) to align projected 3D meshes

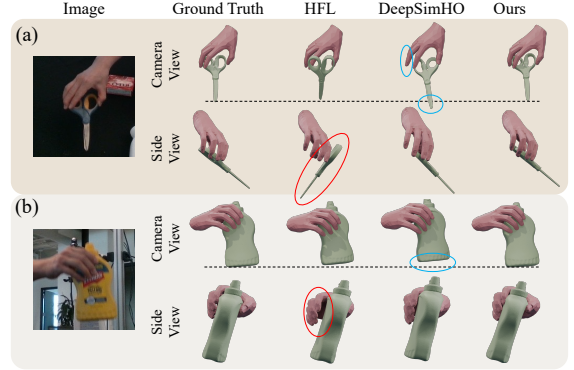


Figure 1: Visual comparison between a state-of-the-art visual-only method, HFL, and a method that incorporates physical cues, DeepSimHO. HFL yields visually aligned yet physically implausible results (red circles), while DeepSimHO improves physical plausibility at the cost of visual alignment (blue circles).

with 2D segmentation masks, while photometric consistency across frames is explored in (Hasson et al. 2020). However, these visual-based methods often neglect physical constraints, leading to physically implausible artifacts such as penetration or lack of contact. As illustrated in Figure 1, the result from HFL (Lin et al. 2023) appears visually reasonable in the original camera view but reveals improper grasping when rendered from a different viewpoint, as highlighted in the red circle.

To improve physical plausibility, several works (Brahmbhatt et al. 2020; Chen et al. 2022; Yang et al. 2024a) introduce post-optimization strategies that incorporate physical constraints. While effective at reducing artifacts such as interpenetration or missing contacts, these methods are highly sensitive to the quality of the initial pose and often produce unstable or suboptimal outputs when the initialization is inaccurate. To better balance visual and physical fidelity, more recent approaches (Hasson et al. 2019; Ehsani et al. 2020; Yang et al. 2024b; Cho et al. 2023; Wang, Mao, and Li 2023a; Hu et al. 2024a) propose end-to-end training methods that incorporate physical cues. While this integra-

*Corresponding author

Copyright © 2026, Association for the Advancement of Artificial Intelligence (www.aaai.org). All rights reserved.

tion improves physical plausibility, it often comes at the cost of degraded visual consistency. As shown in Figure 1, DeepSimHO (Wang, Mao, and Li 2023a) improves physical realism over its visual-only baseline (Yang et al. 2022); yet, the predicted object pose deviates from the image observation (blue circle), compromising pose accuracy.

To resolve these limitations, we propose a novel approach that effectively integrates visual and physical cues to ensure both visual consistency and physical plausibility. This is accomplished through two key ideas: 1) Joint visual-physical cue learning: Our model is trained to extract 2D visual cues (e.g., hand and object heatmaps) alongside 3D physical cues (e.g., force vectors), enabling richer representation learning for hand-object interactions. 2) Candidate pose aggregation: We propose a novel aggregation process that leverages both predicted visual and physical cues to aggregate multiple candidate poses generated by a diffusion model into a single, physically plausible and visually consistent estimate.

A core challenge lies in the prediction of 3D interaction forces due to: (1) their high dimensionality, (2) the complexity of contact dynamics and friction modeling, and (3) the lack of ground-truth force annotations. To address this, we introduce a **Force Prediction Module** that models local contact forces using friction cones and transforms them from local to global coordinates to compute the overall hand-object interaction force. The module is trained via a semi-supervised strategy using physical constraints and pseudo force labels, without requiring ground-truth annotations.

Pose aggregation also poses unique challenges due to the high degrees of freedom of the pose parameters (e.g., articulated hand joints) and the interdependence of hand-object interaction. To address this, we propose a two-stage aggregation scheme: 1) **Visual-based Aggregation**: Candidates are hierarchically aggregated along the kinematic chain using visual cues, which effectively reduces error accumulation and enhances visual consistency. 2) **Physics-based Aggregation**: Candidates are ranked and selected based on physical constraints, such as contact and torque balance, which improves contact quality and enhances physical plausibility.

In summary, the contributions of this work are as follows:

- We propose a novel hand-object pose estimation approach that integrates both visual and physical cues without compromising either.
- We introduce a force prediction module that models interaction forces via friction cones and local-to-global transformation, trained with physical constraints and pseudo force labels.
- We propose a two-stage pose aggregation strategy that leverages both visual and physical cues to yield accurate and physically plausible hand-object poses.

Extensive experiments on standard benchmarks demonstrate that our method achieves state-of-the-art performance in both pose accuracy and physical plausibility.

Related Works

Most existing efforts (Xu et al. 2023; Hasson et al. 2020; Tse et al. 2022a; Zhou et al. 2024; Potamias et al. 2025) es-

timate hand and object poses primarily by leveraging image-based visual cues, ensuring alignment between the 2D projections of the estimated 3D poses and the corresponding image observations. Several methods (Qi et al. 2024; Zhang et al. 2024; Xu et al. 2023) incorporate segmentation losses to enforce consistency between the projected 3D mesh and 2D image segmentations. Similarly, Park et al. (Park et al. 2022) employ a transformer module to inject hand information into occluded 2D regions. However, these methods predominantly focus on visual information and do not explicitly incorporate physical constraints, making them susceptible to physically implausible predictions such as interpenetration or lack of contact.

To address this limitation, several methods (Grady et al. 2021; Yang et al. 2024a; Zhao et al. 2024) propose post-optimization strategies that refine initial pose estimates by incorporating physical cues. For instance, Grady et al. (Grady et al. 2021) and Tse et al. (Tse et al. 2022b) infer desirable hand-object contact regions from initial poses and subsequently optimize both the hand and object to better conform to these inferred regions. Similarly, Hu et al. (Hu et al. 2022) refine hand-object interactions by adjusting fingertip forces and contact points based on initial motion trajectories. While these methods are effective in improving physical plausibility, they rely heavily on accurate initializations. Inaccurate initial poses can cause divergence from visual evidence, resulting in visually inconsistent estimations.

More recently, several studies have explored the unification of visual and physical reasoning within an end-to-end learning framework (Hasson et al. 2019; Cho et al. 2023; Wang, Mao, and Li 2023a; Hu et al. 2024a). Hu et al. (Hu et al. 2024b) model part-level and vertex-level contact probabilities to construct an implicit neural representation of the object, thereby facilitating object pose inference. Wang et al. (Wang, Mao, and Li 2023a) incorporate a physics engine into the training loop to supervise the learning of stability-aware poses based on simulated physical outcomes. While these methods represent progress toward unified visual-physical modeling, they often compromise visual fidelity in favor of physical plausibility. In contrast, our approach integrates visual and physical cues during inference by aggregating multiple candidate poses generated by a diffusion model, enabling the selection of solutions that are both visually consistent and physically plausible.

Following (Lin et al. 2023; Qi et al. 2024), we focus on estimating both hand pose and object 6D pose from a single RGB image, with camera intrinsics and the object CAD model being available. Methods such as (Prakash et al. 2024), which reconstruct only the mesh of the manipulated object without estimating either the hand pose or object 6D pose, are therefore not considered in our comparison.

Method

The framework of our approach is illustrated in Figure 2.

Feature Extraction

Given an input RGB image, an enhanced ResNet50 backbone network (Lin et al. 2023) is employed to extract features for both the hand and the object. These features are

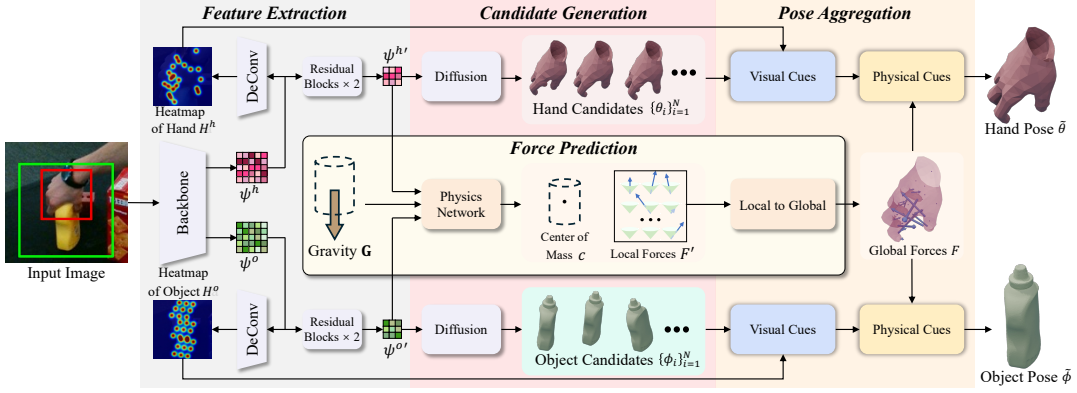


Figure 2: The framework of our approach, consisting of the following four modules: feature extraction, force prediction, candidate generation and pose aggregation.

subsequently processed by DeConv layers (Xiao, Wu, and Wei 2018) to generate the hand heatmap H^h and the object heatmap H^o , which serve as visual cues in pose aggregation module. Two residual blocks (He et al. 2016) further refine the hand and object features, preparing them for force prediction and candidate pose generation. The loss function used to supervise the heatmap predictions is defined as:

$$\mathcal{L}_{hm} = \lambda_{hm} (\mathcal{L}_{mse}(H^h, \bar{H}^h) + \mathcal{L}_{mse}(H^o, \bar{H}^o)), \quad (1)$$

where \mathcal{L}_{mse} denotes the mean square error loss function, $H^h \in \mathbb{R}^{|J^h| \times h_m \times w_m}$ and $\bar{H}^h \in \mathbb{R}^{|J^h| \times h_m \times w_m}$ represent the predicted and ground truth heatmaps for the hand joints J^h , respectively. $H^o \in \mathbb{R}^{|J^o| \times h_m \times w_m}$ and $\bar{H}^o \in \mathbb{R}^{|J^o| \times h_m \times w_m}$ represent the predicted and ground truth heatmaps for the object keypoints J^o , respectively. h_m and w_m denote the height and width of the heatmap, and λ_{hm} is a hyperparameter that weights the heatmap loss. Detailed settings of all hyperparameters are provided in the extended version.

Force Prediction

We focus on hand-object pose estimation from a single image, where motion-related quantities such as acceleration cannot be inferred. Thus, we adopt the static equilibrium assumption as a necessary simplification, which is shown to be effective in our ablation studies.

Local Force Hand-object contact interactions are inherently complex (Hu et al. 2022). Following (Yang et al. 2024a), we approximate this complexity by representing contact forces through 32 sparse anchor points $\{O_k^a\}_{k=1}^{32}$ on the hand surface. Each anchor point O_k^a is associated with a local coordinate system, as depicted in Figure 3(a). According to Coulomb’s friction law (Morin 2008), contact forces must lie within a friction cone determined by a friction coefficient μ . We model this cone using a set of base vectors $\{v_j\}_{j=1}^{N_v}$, where each vector is defined as:

$$v_j = \left(\mu \sin\left(\frac{2\pi j}{N_v}\right), \mu \cos\left(\frac{2\pi j}{N_v}\right), 1 \right). \quad (2)$$

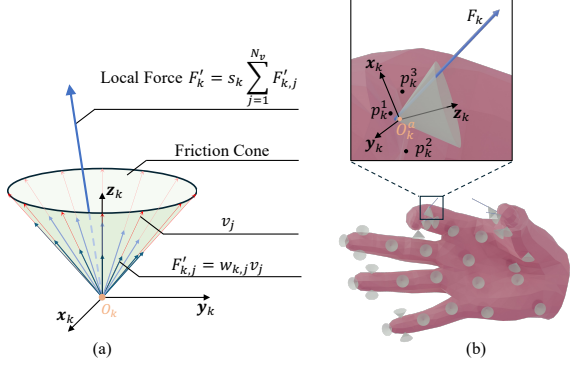


Figure 3: Friction cone and force representations in (a) local and (b) global coordinate frames.

The local force F'_k at anchor point O_k^a is expressed as a weighted sum of these base vectors:

$$F'_k = s_k \sum_{j=1}^{N_v} w_{k,j} v_j, \quad (3)$$

where $s_k \in \mathbb{R}$ and $w_{k,j} \in \mathbb{R}$ are the learned scaling and weighting coefficients, respectively.

Global Force As illustrated in Figure 3(b), the local force F'_k is transformed into a global force F_k using the MANO hand model (Romero, Tzionas, and Black 2017) through its linear blend skinning procedure. Each anchor point $\{O_k^a\}$ is attached to a triangle $\{\triangle p_k^1 p_k^2 p_k^3\}$ on the hand mesh vertices V^h . The transformation is defined as:

$$\begin{cases} F_k = \mathbf{R}_k^{L2G} F'_k, \\ O_k^a = \sum_{i \in \{1,2,3\}} \alpha_k^i p_k^i. \end{cases} \quad (4)$$

Here F'_k and F_k represent the local and global force for the anchor point O_k^a , respectively. $\mathbf{R}_k^{L2G} = [\mathbf{x}_k, \mathbf{y}_k, \mathbf{z}_k]$ denotes

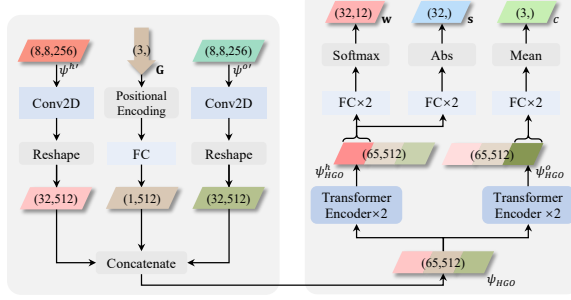


Figure 4: The architecture of our physics network.

the rotation matrix, \mathbf{x}_k is calculated by normalizing the vector $\mathbf{p}_k^2 - \mathbf{p}_k^1$, \mathbf{z}_k is calculated by normalizing the vector $(\mathbf{p}_k^2 - \mathbf{p}_k^1) \times (\mathbf{p}_k^3 - \mathbf{p}_k^2)$, and $\mathbf{y}_k = \mathbf{z}_k \times \mathbf{x}_k$. O_k^a is the weighted sum of $\{p_k^i\}$, and α_k^i is the weight coefficient.

Physical Constraints Given the static equilibrium assumption (Morin 2008), all forces acting on the object must collectively satisfy Newtonian physical constraints. These constraints are used both to train the force prediction module and to guide the pose aggregation process.

Force balance: the sum of all external forces acting on it must be zero. This leads to the force balance constraint,

$$\mathcal{L}_{force} = \left\| \sum_{k=1}^{32} F_k + \mathbf{G} \right\|_2^2, \quad (5)$$

where \mathbf{G} represents the gravity vector. Following (Hu et al. 2022), the magnitude of \mathbf{G} is set to a relative value of 1N.

Torque balance: the sum of all torques acting on it must be zero. Thus, the torque balance constraint is formulated as,

$$\mathcal{L}_{torque} = \left\| \sum_{k=1}^{32} F_k \times r_k \right\|_2^2, \quad (6)$$

Here r_k refers to the position vector of the k -th anchor point, and \times is a cross product between the two vectors.

Contact-force Relation: In hand-object interaction, an anchor point can exert force on an object only if it is in contact with the object’s surface. Consequently, the magnitude of the contact force should be constrained based on the contact state between the anchor and the object. The distance between an anchor point and the object’s surface serves as a key indicator of this contact state. Specifically, a shorter distance implies a higher likelihood of contact, whereas a larger distance suggests a lower probability of contact. Inspired by this, we approximate the contact-force constraint as

$$\mathcal{L}_{contact} = \sum_{k=1}^{32} \|F_k\|_2 \cdot |d_k|, \quad (7)$$

where $|d_k|$ denotes the distance between the anchor point and the object’s surface, and $\|F_k\|_2$ represents the magnitude of the force. This constraint is an essential physical cue for our physics-based aggregation.

Physics Network As illustrated in Figure 4, our physics network takes 1) the hand feature ψ^h , 2) the object feature ψ^o , and 3) the gravity vector $\mathbf{G} \in \mathbb{R}^3$ as inputs. During training, \mathbf{G} is aligned vertically downward with respect to the tabletop. During inference, we approximate \mathbf{G} using the camera’s y-axis, as in (Wang, Mao, and Li 2023a). The network outputs 1) the weight matrix $\mathbf{w} \in \mathbb{R}^{32 \times N_v}$, 2) the scaling vector $\mathbf{s} \in \mathbb{R}^{32}$, and 3) the object center-of-mass position $\mathbf{c} \in \mathbb{R}^3$. The predicted local force F'_k is computed using \mathbf{w} and \mathbf{s} as defined in Equation 3. The network is supervised using the following loss:

$$\begin{aligned} \mathcal{L}_{phy} = & \lambda_F \mathcal{L}_{mse}(F', \tilde{F}') + \lambda_c \mathcal{L}_{mse}(c, \bar{c}) \\ & + \lambda_{force} \mathcal{L}_{force} + \lambda_{torque} \mathcal{L}_{torque}, \end{aligned} \quad (8)$$

where F' and \tilde{F}' are the predicted forces and pseudo force labels, c and \bar{c} are the predicted and ground-truth object center-of-mass positions, λ_F , λ_c , λ_{force} , and λ_{torque} are hyperparameters balancing the loss terms. The pseudo force labels \tilde{F}' are precomputed via an optimization process constrained by the physical constraints, further details are provided in the extended version.

Pose Aggregation

Given a set of candidate hand poses $\{(\theta_i, \beta_{reg})\}_{i=1}^N$, where $\theta_i \in \mathbb{R}^{16 \times 3}$ are the MANO pose parameters of 16 hand joints and $\beta_{reg} \in \mathbb{R}^{10}$ is the MANO shape parameter, and a set of rigid object pose candidates, where $\{(R_i, T_i)\}_{i=1}^N$, $R_i \in \mathbb{R}^3$, $T_i \in \mathbb{R}^3$ represent rotation and translation respectively, the pose aggregation module is designed to refine these candidates through two sequential stages: visual-based aggregation and physics-based aggregation, as illustrated in Figure 2. The initial pose candidates are generated by a candidate generation module based on a score-based diffusion model (Song et al. 2021). Further details of this module are provided in the extended version.

Visual-based Aggregation In articulated systems such as the human hand, higher-level joint positions depend on lower-level ones due to kinematic dependencies. Consequently, errors tend to accumulate across levels, leading to increasingly inaccurate joint predictions at higher levels. To address this, we propose a level-by-level aggregation strategy that progressively refines joint parameters from lower to higher levels using heatmaps as visual guidance. As shown in Figure 5(a), hand joints with degrees of freedom are categorized into four hierarchical levels, with the index set of joints at level l denoted by L_l . The aggregation proceeds iteratively from level 1 to level 4 (Figure 5(b)). After aggregating each level, the refined joint parameters are used to overwrite the corresponding joints across all candidate poses. This reduces the propagation of errors to higher levels. For the j -th joint in level L_l , we compute a visual score s_i^h for each hand pose candidate (θ_i, β_{reg}) using the following formula:

$$s_i^h = \sum_{c \in Children_j} H_c^h \left(\text{Proj2D}^h(c, \theta_i, \beta_{reg}) \right), \quad (9)$$

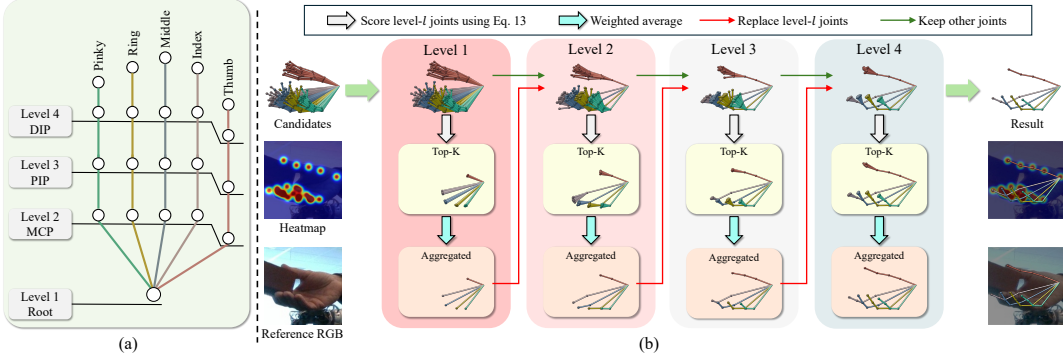


Figure 5: (a) The levels of hand pose parameters; (b) The visual-based aggregation hierarchically aggregate hand joints from lower to higher levels.

where $Children_j$ denotes the set of higher-level joints within the same kinematic chain as joint j , $\text{Proj2D}^h(\cdot)$ denotes the 2D projection of the c -th joint for candidate (θ_i, β_{reg}) , and $H_c^h(\cdot)$ retrieves the heatmap value at the projected 2D location for joint c . Using these scores $\{s_i^h\}_{i=1}^N$, the top-K candidates $\{\theta_i\}_{i \in K^h}$ are selected. The aggregated pose parameter for joint j , denoted by $\tilde{\theta}[j, :]$, is computed as the weighted average of the selected candidates:

$$\tilde{\theta}[j, :] = \frac{\sum_{i \in K^h} s_i^h \theta_i[j, :] \cdot s_i^h}{\sum_{i \in K^h} s_i^h}. \quad (10)$$

This aggregated value then replaces all $\theta_i[j, :]$ for $i = 1, \dots, N$. This process is repeated for each level until all hand pose parameters are aggregated.

The same principle is applied to object pose aggregation. Object pose parameters are separated into two levels: 1) the translation parameter T_o , and 2) the rotation parameters R_o . The visual score for each object candidate is computed using:

$$s_i^o = \sum_{c=1}^{27} H_c^o(\text{Proj2D}^o(c, R_i, T_i)), \quad (11)$$

where $\text{Proj2D}^o(c, R_i, T_i)$ is the 2D projection of the c -th object keypoint after applying transformation (R_i, T_i) to the object model, and $H_c^o(\cdot)$ retrieves the heatmap value at the projected 2D location. Object translation parameters are aggregated first and used to overwrite the translation parameters of all candidates. Rotation parameters are subsequently aggregated using the updated translations.

Physics-based Aggregation To further enhance the physical plausibility of the hand-object interaction, we introduce a physics-based aggregation step that utilizes physical constraints to guide candidate pose aggregation. For the hand, we compute a physics-based score as:

$$s_{phy}^h = -\mathcal{L}_{force} \cdot \mathcal{L}_{contact}. \quad (12)$$

We focus on refining the joints at the highest hierarchy level L_4 . Let K_4^h denote the top-K hand pose candidates previously aggregated at level L_4 . We collect joint parameters

Method	Hand		Object		
	MJE	PA-MJE	MCE	OCE	ADDS
Liu et al. (2021)	15.2	6.58	-	-	-
HandOccNet (2022)	14.0	5.80	-	-	-
H2ONet (2023)	14.0	5.70	-	-	-
HandBooster (2024)	11.9	5.2	-	-	-
SimpleHand (2024)	12.4	5.5	-	-	-
HFL (2023)	12.6	5.47	48.0	42.7	33.8
HOISDF (2024)	10.1	5.13	35.8	27.6	18.6
Ours	10.0	5.08	26.2	23.7	13.5

Table 1: Comparison of pose accuracy on *DexYCB Full* (metrics are in mm).

Method	Hand		Object	
	PA-MJE	MJE	OCE	ADDS
Hasson et al. (2019)	11.0	-	67.0	22.0
Hasson et al. (2020)	11.4	-	80.0	40.0
Hampali et al. (2022)	10.8	25.5	68.0	21.4
Liu et al. (2021)	10.1	-	-	-
DMA (2023b)	10.1	23.8	45.5	20.8
HFL (2023)	8.9	28.9	64.3	32.4
HandBooster (2024)	8.5	21.1	-	-
LCP (2024)	8.5	21.5	-	-
HOISDF (2024)	9.2	19.0	35.5	14.4
Ours w/o pretraining	8.9	21.1	29.3	15.2
Ours	8.5	19.9	27.1	14.3

Table 2: Comparison of pose accuracy on *HO3Dv2 Full* (metrics are in mm).

$\{\theta_i[j, :]\}_{i \in K_4^h, j \in L_4}$ and re-rank them based on their physics-based scores computed using Equation 12. The top-K joint parameters $\{\theta_n[j, :]\}_{n \in K_{phy}^h}$ are then averaged to produce the final hand pose estimates for level L_4 . For the object, the physics-based score is defined as:

$$s_{phy}^o = -\mathcal{L}_{torque} \cdot \mathcal{L}_{contact}. \quad (13)$$

Method	Hand MJE \downarrow	Object SMCE \downarrow	Physics		
			CP(%) \uparrow	PD \downarrow	SD \downarrow
Ground Truth	-	-	100	9.1	6.4
Hasson et al. (2020)	12.5	-	84.35	18.0	48.3
DMA (2023b)	11.5	-	89.16	15.7	35.3
ArtiBoost (2022)	10.7	16.0	94.23	15.0	27.8
DeepSimHO (2023a)	11.2	17.3	95.90	14.8	24.2
Ours	8.5	15.1	98.85	13.4	17.3

Table 3: Comparison of hand-object physics plausibility on *DexYCB Phy* (metrics, except CP, are in mm).

We retrieve the top-K translation candidates $\{T_i\}_{i \in K_T^o}$ and top-K rotation candidates $\{R_j\}_{j \in K_R^o}$ from the visual-based aggregation stage. These components are then combined to form a new set of object pose candidates $\{(T_i, R_j)\}_{i \in K_T^o, j \in K_R^o}$. Each pair is scored using Equation 13, and the top-K combinations $\{(T_n, R_m)\}_{(n, m) \in K_{\text{phy}}^o}$ are selected. The final object pose is obtained by averaging these top-ranked pose pairs. The analysis of the number of candidates and the top-K size is provided in the extended version.

Experiments

Our method is compared against state-of-the-art approaches on two widely used benchmarks: DexYCB (Chao et al. 2021) and HO3D v2 (Hampali et al. 2020).

DexYCB: To train the model, the training set of official “S0” split (Chao et al. 2021) is employed. To evaluate the pose estimation accuracy, two common testing sets are used: *DexYCB Full*, the testing set of official “S0” split, includes scenarios of hands approaching objects as well as hands contacting objects; To evaluate the physical plausibility of the results, following (Wang, Mao, and Li 2023a), *DexYCB Phy* is employed as the testing set, in which the hands steadily hold the object.

HO3Dv2: To train the model, the standard training set is employed. To evaluate the pose estimation accuracy, standard testing set *HO3Dv2 Full* is used. To evaluate the physical plausibility of the results, following (Wang, Mao, and Li 2023a; Yang et al. 2024a), *HO3Dv2 Phy* is employed as the testing set, whose physics plausibility is manually verified by (Yang et al. 2024a). Some methods use additional data to train their models (Qi et al. 2024; Pavlakos et al. 2024; Xu et al. 2023; Wang, Mao, and Li 2023b). Following (Xu et al. 2023), we optionally pretrain on DexYCB for 5 epochs and report results both with and without this pretraining.

Evaluation Metrics

Pose Metrics: For hand, Mean Joint Error (MJE) and Procrustes aligned Mean Joint Error (PA-MJE) are reported. For object, Object Center Error (OCE), Mean Corner Error (MCE), Symmetry-aware Mean Corner Error (SMCE), and average closest point distance (ADD-S) are evaluated.

Physics Metrics: The contact percentage (CP) is calculated to assess the ratio of predictions with hand-object contact.

Method	Object SMCE \downarrow	Physics		
		CP(%) \uparrow	PD \downarrow	SD \downarrow
Hasson et al. (2020)	5.35	78.52	2.02	6.40
CPF (2024a)	5.74	96.47	1.65	3.16
DMA (2023b)	4.79	93.07	1.88	3.47
ArtiBoost (2022)	4.86	94.47	1.27	2.83
DeepSimHO (2023a)	5.28	96.64	1.17	2.42
Ours	3.12	98.80	0.96	2.21

Table 4: Comparison of hand-object physics plausibility on *HO3Dv2 Phy* (metrics, except CP, are in cm).

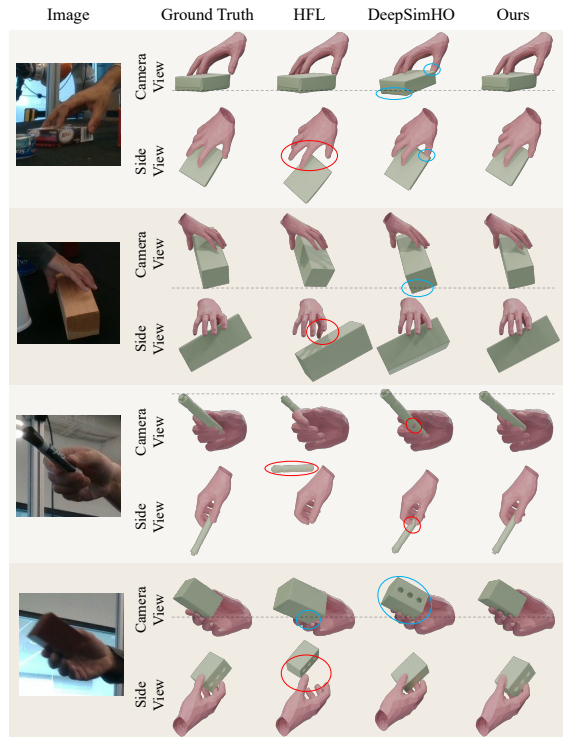


Figure 6: Qualitative results on *DexYCB Phy*. Red circles indicate incorrect hand object interaction. Blue circles point out the incorrect pose estimation. For more qualitative results, please refer to the extended version.

The penetration depth (PD) is used to measure the maximum penetration distance between hand and object predictions. To evaluate the stability of hand holding object, the simulation displacement (SD) (Wang, Mao, and Li 2023a) is used to compute the average object center displacement after 200ms in the virtual physical simulator.

Pose Estimation Accuracy

The proposed method is compared with the state-of-the-art pose estimation methods, including both hand-object pose estimators (Hasson et al. 2019; Kuang, Ding, and Yao 2024; Hasson et al. 2021; Chen et al. 2023; Yang et al. 2022; Wang, Mao, and Li 2023b; Hasson et al. 2020; Liu et al. 2021; Lin

Force Prediction	Visual-based Aggregation	Physics-based Aggregation	Hand		Object		Physics		
			MJE \downarrow	PA-MJE \downarrow	OCE \downarrow	ADDS \downarrow	CP(%) \uparrow	PD \downarrow	SD \downarrow
✓			12.54	5.45	35.30	20.14	95.42	14.4	30.4
✓	✓		12.16	5.33	29.81	16.66	96.51	14.1	25.9
✓	✓	✓	10.05	5.09	26.12	15.21	97.95	13.9	20.0
			10.01	5.08	23.72	13.47	98.85	13.4	17.3

Table 5: Ablation study (metrics, except CP, are in mm). Hand and object metrics are evaluated on *DexYCB Full*. Physics metrics are evaluated on *DexYCB Phy*.

et al. 2023; Qi et al. 2024) and hand pose estimators (Park et al. 2022; Hampali et al. 2022; Xie et al. 2024; Xu et al. 2023, 2024; Zhou et al. 2024).

The results on *DexYCB Full* are shown in Table 1. The proposed method outperforms the compared methods on both hand and object estimation. Especially in terms of object metrics, the proposed method significantly outperforms the second best with reducing the error of MCE, OCE and ADDS by 26.8%, 14.1%, and 27.4%, respectively.

The results on *HO3Dv2 Full* are shown in Table 2. Compared with the state-of-the-art methods, the proposed method achieves better performance on joint hand-object pose estimation. For the hand-related metrics, the proposed method is comparable to state-of-the-art methods. For object-related metrics, the proposed method achieves the best performance.

Physical Plausibility

The proposed method is compared with physics-based methods (Wang, Mao, and Li 2023a; Yang et al. 2024a; Hasson et al. 2021), and visual-based methods (Yang et al. 2022; Wang, Mao, and Li 2023b).

The results on *DexYCB Phy* are shown in Table 3. Among the existing methods, DeepSimHO (Wang, Mao, and Li 2023a) achieves the best physical performance, but its accuracy on hand and object is suboptimal. Comparing to DeepSimHO, ArtiBoost (Yang et al. 2022) has better pose estimation accuracy, but its physical plausibility is inferior. The existing methods cannot balance on both physics and pose estimation. In contrast, the proposed method significantly outperforms existing methods in both physical plausibility and pose accuracy.

The results on *HO3Dv2 Phy* are shown in Table 4. Our method achieves state-of-the-art performance across all physics metrics. Compared to the strongest baseline, DeepSimHO, our method further reduces PD and SD while improving contact rate and object accuracy, demonstrating the effectiveness of our approach in producing both physically plausible and accurate poses.

The qualitative results are shown in Figure 6. The visual-based method HFL (Lin et al. 2023) appears to have good visual consistency in the camera view. However, in the side view, incorrect hand-object interactions are observed. Compared to HFL, the physics-based method DeepSimHO (Wang, Mao, and Li 2023a) has more plausible hand-object interaction but less visual consistency in the front view. Comparing to these methods, the proposed

method achieves better performance on both visual consistency and physical plausibility. For more qualitative results, please refer to the extended version.

Ablation Study

The experimental results of ablation study are shown in Table 5. Starting from the baseline with no force prediction or aggregation modules, the model exhibits the weakest performance across hand, object, and physics metrics. Introducing the force prediction module alone yields modest improvements, particularly in object pose accuracy (OCE drops from 35.30 mm to 29.81 mm, and ADD-S from 20.14 mm to 16.66 mm), indicating that learning physical cues already aids hand-object pose quality. Adding the visual-based aggregation further improves both hand and object metrics (MJE reduced to 10.05 mm, OCE to 26.12 mm), demonstrating its effectiveness in reducing error accumulation. Finally, the inclusion of the physics-based aggregation module yields the best overall results. It achieves the lowest errors across all metrics, particularly in physics-based evaluations: CP increases from 97.95% to 98.85%, while PD and SD drop from 13.9 mm to 13.4 mm and from 20.0 mm to 17.3 mm, respectively. These gains confirm the effectiveness of the proposed physics-based aggregation strategy in enhancing physical plausibility for hand-object pose estimation results. Additional analyses of aggregation strategies, inference-time efficiency, and the influence of candidate quantity and Top-K selection are provided in the extended version.

Conclusion

In this paper, we have presented a novel approach for hand-object pose estimation that effectively combines visual and physical cues to tackle the inherent challenges of visual consistency and physical plausibility in existing methods. Our method learns not only 2D visual representations but also 3D physical cues, using a semi-supervised learning strategy combined with a local-to-global transformation mechanism. The predicted visual and physical cues guide a candidate pose aggregation module, enabling the aggregation of physically plausible and visually coherent hand-object poses. Our experimental results demonstrate that the proposed framework achieves state-of-the-art performance in both pose estimation accuracy and physical plausibility. Future work includes incorporating temporal information to model dynamic equilibrium in hand-object interactions and leveraging physical cues to improve object reconstruction.

Acknowledgments

This work was supported by the National Natural Science Foundation of China under Grant 62273318, the Science and Technology Project funds of Power Construction Corporation of China Ltd., and the Science and Technology Project of Sinohydro Bureau 8 Company Ltd.

References

Billard, A.; and Kragic, D. 2019. Trends and challenges in robot manipulation. *Science*, 364(6446): eaat8414.

Brahmbhatt, S.; Tang, C.; Twigg, C. D.; Kemp, C. C.; and Hays, J. 2020. ContactPose: A Dataset of Grasps with Object Contact and Hand Pose. In *ECCV*.

Chao, Y.-W.; Yang, W.; Xiang, Y.; Molchanov, P.; Handa, A.; Tremblay, J.; Narang, Y. S.; Van Wyk, K.; Iqbal, U.; Birchfield, S.; Kautz, J.; and Fox, D. 2021. DexYCB: A Benchmark for Capturing Hand Grasping of Objects. In *CVPR*.

Chen, Y.; Wang, Q.; Chen, H.; Song, X.; Tang, H.; and Tian, M. 2019. An overview of augmented reality technology. *Journal of Physics: Conference Series*, 1237(2): 022082.

Chen, Z.; Chen, S.; Schmid, C.; and Laptev, I. 2023. gSDF: Geometry-Driven Signed Distance Functions for 3D Hand-Object Reconstruction. In *CVPR*.

Chen, Z.; Hasson, Y.; Schmid, C.; and Laptev, I. 2022. AlignSDF: Pose-Aligned Signed Distance Fields for Hand-Object Reconstruction. In *ECCV*.

Cho, H.; Kim, C.; Kim, J.; Lee, S.; Ismayilzada, E.; and Baek, S. 2023. Transformer-Based Unified Recognition of Two Hands Manipulating Objects. In *CVPR*.

Dormand, J.; and Prince, P. 1980. A family of embedded Runge-Kutta formulae. *Journal of Computational and Applied Mathematics*, 6(1): 19–26.

Ehsani, K.; Tulsiani, S.; Gupta, S.; Farhadi, A.; and Gupta, A. 2020. Use the Force, Luke! Learning to Predict Physical Forces by Simulating Effects. In *CVPR*.

Grady, P.; Tang, C.; Twigg, C. D.; Vo, M.; Brahmbhatt, S.; and Kemp, C. C. 2021. ContactOpt: Optimizing Contact to Improve Grasps. In *CVPR*.

Hampali, S.; Rad, M.; Oberweger, M.; and Lepetit, V. 2020. HOnnote: A Method for 3D Annotation of Hand and Object Poses. In *CVPR*.

Hampali, S.; Sarkar, S. D.; Rad, M.; and Lepetit, V. 2022. Keypoint Transformer: Solving Joint Identification in Challenging Hands and Object Interactions for Accurate 3D Pose Estimation. In *CVPR*.

Hasson, Y.; Tekin, B.; Bogo, F.; Laptev, I.; Pollefeys, M.; and Schmid, C. 2020. Leveraging Photometric Consistency Over Time for Sparsely Supervised Hand-Object Reconstruction. In *CVPR*.

Hasson, Y.; Varol, G.; Schmid, C.; and Laptev, I. 2021. Towards Unconstrained Joint Hand-Object Reconstruction From RGB Videos. In *3DV*.

Hasson, Y.; Varol, G.; Tzionas, D.; Kalevatykh, I.; Black, M. J.; Laptev, I.; and Schmid, C. 2019. Learning Joint Reconstruction of Hands and Manipulated Objects. In *CVPR*.

He, K.; Zhang, X.; Ren, S.; and Sun, J. 2016. Deep Residual Learning for Image Recognition. In *CVPR*.

Hu, H.; Yi, X.; Cao, Z.; Yong, J.-H.; and Xu, F. 2024a. Hand-Object Interaction Controller (HOIC): Deep Reinforcement Learning for Reconstructing Interactions with Physics. In *SIGGRAPH*.

Hu, H.; Yi, X.; Zhang, H.; Yong, J.-H.; and Xu, F. 2022. Physical Interaction: Reconstructing Hand-object Interactions with Physics. In *SIGGRAPH Asia*.

Hu, J.; Zhang, H.; Chen, Z.; Li, M.; Wang, Y.; Liu, Y.; and Sun, Z. 2024b. Learning Explicit Contact for Implicit Reconstruction of Hand-held Objects from Monocular Images. In *AAAI*.

Kuang, Z.; Ding, C.; and Yao, H. 2024. Learning Context with Priors for 3D Interacting Hand-Object Pose Estimation. In *MM*.

Lin, Z.; Ding, C.; Yao, H.; Kuang, Z.; and Huang, S. 2023. Harmonious Feature Learning for Interactive Hand-Object Pose Estimation. In *CVPR*.

Liu, S.; Jiang, H.; Xu, J.; Liu, S.; and Wang, X. 2021. Semi-Supervised 3D Hand-Object Poses Estimation With Interactions in Time. In *CVPR*.

Morin, D. 2008. *Introduction to classical mechanics: with problems and solutions*. Cambridge University Press.

Mueller, F.; Davis, M.; Bernard, F.; Sotnychenko, O.; Verschoor, M.; Otaduy, M. A.; Casas, D.; and Theobalt, C. 2019. Real-time pose and shape reconstruction of two interacting hands with a single depth camera. *ACM Transactions on Graphics*, 38(4).

Narasimhaswamy, S.; Nguyen, H. A.; Huang, L.; and Hoai, M. 2024. HOIST-Former: Hand-held Objects Identification Segmentation and Tracking in the Wild. In *CVPR*.

Park, J.; Oh, Y.; Moon, G.; Choi, H.; and Lee, K. M. 2022. HandOccNet: Occlusion-Robust 3D Hand Mesh Estimation Network. In *CVPR*.

Pavlakos, G.; Shan, D.; Radosavovic, I.; Kanazawa, A.; Fouhey, D.; and Malik, J. 2024. Reconstructing Hands in 3D with Transformers. In *CVPR*.

Potamias, R. A.; Zhang, J.; Deng, J.; and Zafeiriou, S. 2025. WiLoR: End-to-end 3D Hand Localization and Reconstruction in-the-wild. In *CVPR*.

Prakash, A.; Chang, M.; Jin, M.; Tu, R.; and Gupta, S. 2024. 3D Reconstruction of Objects in Hands without Real World 3D Supervision. In *ECCV*.

Qi, H.; Zhao, C.; Salzmann, M.; and Mathis, A. 2024. HOISDF: Constraining 3D Hand-Object Pose Estimation with Global Signed Distance Fields. In *CVPR*.

Ren, F.; and Bao, Y. 2020. A Review on Human-Computer Interaction and Intelligent Robots. *International Journal of Information Technology & Decision Making*, 19(01): 5–47.

Romero, J.; Tzionas, D.; and Black, M. J. 2017. Embodied Hands: Modeling and Capturing Hands and Bodies Together. *ACM Transactions on Graphics*, 36(6).

Song, Y.; and Ermon, S. 2019. Generative Modeling by Estimating Gradients of the Data Distribution. In *Advances in NeurIPS*.

Song, Y.; Sohl-Dickstein, J.; Kingma, D. P.; Kumar, A.; Ermon, S.; and Poole, B. 2021. Score-Based Generative Modeling through Stochastic Differential Equations. In *ICLR*.

Tse, T. H. E.; Kim, K. I.; Leonardis, A.; and Chang, H. J. 2022a. Collaborative Learning for Hand and Object Reconstruction With Attention-Guided Graph Convolution. In *CVPR*.

Tse, T. H. E.; Zhang, Z.; Kim, K. I.; Leonardis, A.; Zheng, F.; and Chang, H. J. 2022b. S²Contact: Graph-Based Network for 3D Hand-Object Contact Estimation with Semi-supervised Learning. In *ECCV*.

Vincent, P. 2011. A Connection Between Score Matching and Denoising Autoencoders. *Neural Computation*, 23(7): 1661–1674.

Wang, R.; Mao, W.; and Li, H. 2023a. DeepSimHO: Stable Pose Estimation for Hand-Object Interaction via Physics Simulation. In *NeurIPS*.

Wang, R.; Mao, W.; and Li, H. 2023b. Interacting Hand-Object Pose Estimation via Dense Mutual Attention. In *WACV*.

Xiao, B.; Wu, H.; and Wei, Y. 2018. Simple Baselines for Human Pose Estimation and Tracking. In *ECCV*.

Xie, P.; Xu, W.; Tang, T.; Yu, Z.; and Lu, C. 2024. MS-MANO: Enabling Hand Pose Tracking with Biomechanical Constraints. In *CVPR*.

Xu, H.; Li, H.; Wang, Y.; Liu, S.; and Fu, C.-W. 2024. Hand-Booster: Boosting 3D Hand-Mesh Reconstruction by Conditional Synthesis and Sampling of Hand-Object Interactions. In *CVPR*.

Xu, H.; Wang, T.; Tang, X.; and Fu, C.-W. 2023. H2ONet: Hand-Occlusion-and-Orientation-Aware Network for Real-Time 3D Hand Mesh Reconstruction. In *CVPR*.

Yang, L.; Li, K.; Zhan, X.; Lv, J.; Xu, W.; Li, J.; and Lu, C. 2022. ArtiBoost: Boosting Articulated 3D Hand-Object Pose Estimation via Online Exploration and Synthesis. In *CVPR*.

Yang, L.; Zhan, X.; Li, K.; Xu, W.; Zhang, J.; Li, J.; and Lu, C. 2024a. Learning a Contact Potential Field for Modeling the Hand-Object Interaction. *IEEE Transactions on Pattern Analysis and Machine Intelligence*, 46(8): 5645–5662.

Yang, Y.; Zhai, W.; Luo, H.; Cao, Y.; and Zha, Z.-J. 2024b. LEMON: Learning 3D Human-Object Interaction Relation from 2D Images. In *CVPR*.

Zhang, C.; Jiao, G.; Di, Y.; Wang, G.; Huang, Z.; Zhang, R.; Manhardt, F.; Fu, B.; Tombari, F.; and Ji, X. 2024. MOHO: Learning Single-view Hand-held Object Reconstruction with Multi-view Occlusion-Aware Supervision. In *CVPR*.

Zhao, Y.; Kwon, T.; Streli, P.; Pollefeys, M.; and Holz, C. 2024. EgoPressure: A Dataset for Hand Pressure and Pose Estimation in Egocentric Vision. *arXiv*.

Zhou, Z.; Zhou, S.; Lv, Z.; Zou, M.; Tang, Y.; and Liang, J. 2024. A Simple Baseline for Efficient Hand Mesh Reconstruction. In *CVPR*.

Supplementary Material

Abstract

In this supplementary material, we provide additional details about our proposed method, including visualizations of the pseudo force labels and an overview of the diffusion models used to generate hand and object pose candidates. We also describe the hyperparameter settings and analyze the impact of the number of candidates and the top-K selection size on performance. Furthermore, we present extended experiments, such as comparisons of different aggregation strategies and an in-depth analysis of our proposed aggregation scheme. We additionally report comprehensive quantitative metrics for both hand and object pose estimation. Finally, we provide a detailed breakdown of the inference runtime of each module in our framework.

Pseudo Force Label

Pseudo Force Label Generation

To generate the pseudo force labels, we employ physical constraints to optimize the weight matrix $\mathbf{w} \in \mathbb{R}^{32 \times N_v}$ and the scaling vector $\mathbf{s} \in \mathbb{R}^{32}$. To enforce the conditions $\sum_{j=1}^{N_v} w_{ij} = 1$ and $s_k \geq 0$, we optimize instead the matrix $\tilde{\mathbf{w}} \in \mathbb{R}^{32 \times N_v}$ and the vector $\tilde{\mathbf{s}} \in \mathbb{R}^{32}$. The relation between these variables are expressed as follows:

$$\mathbf{w}_k = \text{softmax}(\tilde{\mathbf{w}}_k), \quad s_k = |\tilde{s}_k|, \quad (14)$$

where \mathbf{w}_k and $\tilde{\mathbf{w}}_k$ denote the k -th column of \mathbf{w} and $\tilde{\mathbf{w}}$, respectively, while s_k and \tilde{s}_k refer to the k -th element of \mathbf{s} and $\tilde{\mathbf{s}}$, respectively.

The initial values for $\tilde{\mathbf{s}}$ are determined based on the distance between the hand and the object. Specifically, given the hand and object meshes, we compute the signed distance d_k from the object's surface to the anchor point k . A mapping function Ω is defined to smoothly converts the signed distance d_k to a value between (0, 1):

$$\Omega(d_k) = \frac{1}{(1 + e^{-16(d_k+1)})(1 + e^{-16(d_k-0.75)})}. \quad (15)$$

This function transitions smoothly to 1 for $d_k \in (0, 0.75)$ and approaches 0 otherwise, as illustrated in Fig. 7. If $\Omega(d_k) < 0.1$, we set \tilde{s}_k to a fixed value 0 and keep it unchanged; otherwise, we initialize \tilde{s}_k to a value of 0.05. The initial values for $\{\tilde{w}_{k,j}\}$ are set uniformly to $\frac{1}{N_v}$.

The optimization process includes two phases. In the first phase, the primary objective is to optimize the matrix $\tilde{\mathbf{w}}$, ensuring that the resultant hand force vector acts against the object's gravity. For this purpose, the physical constraint $\mathcal{L}_{\text{force}}$ is employed:

$$\mathcal{L}_{\text{force}} = \left\| \sum_{k=1}^{32} \left(R_k^{L2G} s_k \sum_{j=1}^{N_v} w_{k,j} \mathbf{v}_j \right) - \mathbf{G} \right\|_2^2. \quad (16)$$

The optimization goal for this phase can be formulated as:

$$\arg \min_{\tilde{\mathbf{w}}} \mathcal{L}_{\text{force}}. \quad (17)$$

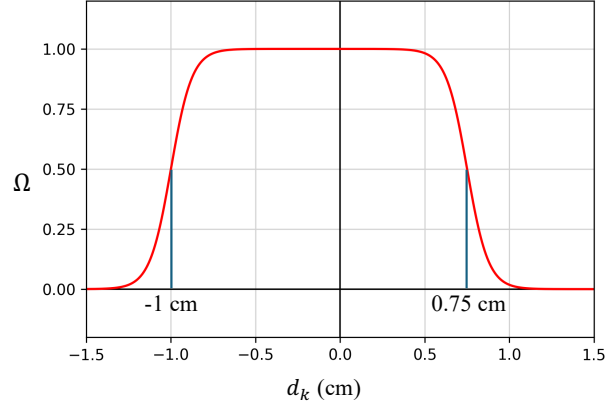


Figure 7: The mapping function $\Omega(d_k)$.

In the second phase, the goal is to minimize the resultant force and torque exerted on the object. Additionally, the process encourages anchor points that are in contact with the object to exert force while reducing the force exerted by anchor points that are farther away. To achieve this goal, the matrix $\tilde{\mathbf{w}}$ and the vector $\tilde{\mathbf{s}}$ are jointly optimized using the loss functions $\mathcal{L}_{\text{force}}$, $\mathcal{L}_{\text{torque}}$, and $\mathcal{L}_{\text{contact2}}$:

$$\arg \min_{\tilde{\mathbf{w}}, \tilde{\mathbf{s}}} (\mathcal{L}_{\text{force}} + 30\mathcal{L}_{\text{torque}} + 0.1\mathcal{L}_{\text{contact2}}). \quad (18)$$

Here, $\mathcal{L}_{\text{force}}$ is used to minimize the resultant force. $\mathcal{L}_{\text{torque}}$ is used to minimize the resultant torque which is defined as:

$$\mathcal{L}_{\text{torque}} = \left\| \sum_{k=1}^{32} \left(R_k^{L2G} s_k \sum_{j=1}^{N_v} w_{k,j} \mathbf{v}_j \right) \times r_k \right\|_2^2. \quad (19)$$

The function $\mathcal{L}_{\text{contact2}}$ is used to encourage anchor points in contact with the object to exert force while suppressing the force from those far away. It is defined as:

$$\mathcal{L}_{\text{contact2}} = \sum_{k=1}^{32} \log^2 \left(\frac{\Omega(d_k) \sqrt{\sum_{i=1}^{32} s_i^2}}{s_k \sqrt{\sum_{i=1}^{32} \Omega^2(d_i)} + \epsilon} \right), \quad (20)$$

where ϵ is a hyperparameter, set to 10^{-5} , to avoid division by zero. In our experiments, we utilize the AdamW optimizer with a learning rate of 10^{-3} . Typically, convergence for the first phase occurs after approximately 300 optimization steps, while the second phase converges after about 2700 steps.

Visualization of Pseudo Force and Predicted Force
The visualization of the pseudo force and predicted force is shown in Figure 8.

Candidate Generation

To generate hand candidates, a candidate generator Θ^h produces a set of plausible MANO hand poses $\{\theta_i\}_{i=1}^N$, where

Num. of Candidates	Top-K Size in VA		Top-K Size in PA		Hand		Object		Complexity	
	Hand	Object	Hand	Object	MJE	PA-MJE	OCE	ADDS	GFLOPs	Params (M)
50	30	10	5	5	10.12	5.14	24.71	14.03	22.41	48.95
100	30	10	5	5	10.01	5.08	23.72	13.47	25.51	48.95
200	30	10	5	5	10.00	5.07	22.75	12.89	31.94	48.95
100	10	10	5	5	10.23	5.24	23.74	13.48	25.51	48.95
100	30	30	5	5	10.01	5.08	24.66	13.68	25.51	48.95
100	60	60	5	5	10.05	5.10	26.29	14.33	25.51	48.95
100	30	10	1	1	10.04	5.11	24.17	13.50	25.51	48.95
100	30	10	5	5	10.01	5.08	23.72	13.47	25.51	48.95
100	30	10	10	10	10.05	5.08	24.40	14.34	25.51	48.95

Table 6: Analysis of candidate number and top-K size on *DexYCB Full*.

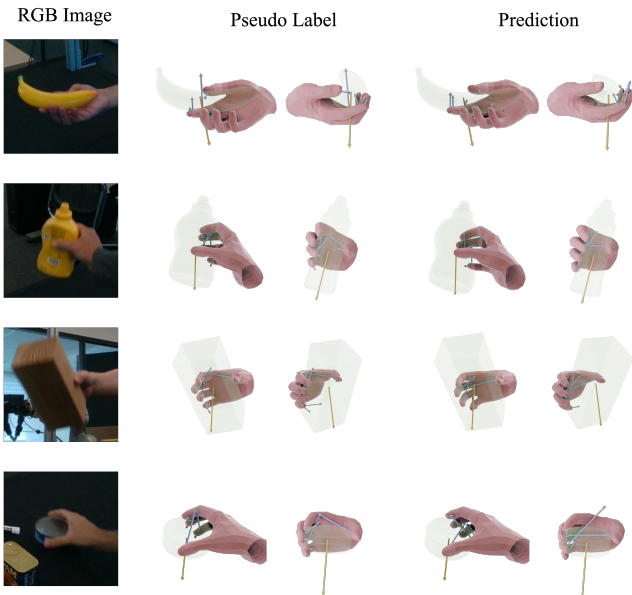


Figure 8: The visualization of the pseudo force label and predicted force. Blue arrows indicate the force vectors, while yellow arrows indicate the gravity vectors.

each $\theta_i \in \mathbb{R}^{16 \times 6}$ represents the continuous 6D rotation representation of the joint angles for the wrist and 15 finger joints. Following previous efforts (Hampali et al. 2022; Lin et al. 2023; Narasimhaswamy et al. 2024), the wrist position is assumed to be known.

The candidate generators for both hands and objects are modeled based on the score-based diffusion model (Song et al. 2021; Song and Ermon 2019). In what follows, we focus on describing the hand candidate generator, as the object candidate generator operates in a similar manner. The diffusion process $\{\theta(t)\}_{t=0}^1$ is constructed using the Variance-Exploding Stochastic Differential Equation (VE-

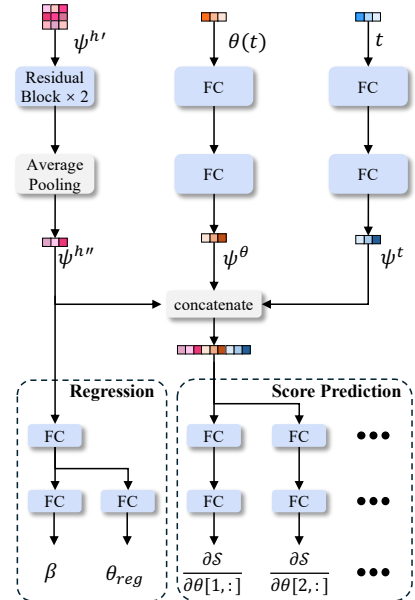


Figure 9: The network architecture of our hand candidate generator.

SDE) (Song et al. 2021),

$$d\theta(t) = \sqrt{\frac{d(\sigma^2(t))}{dt}} dw. \quad (21)$$

Here, w is a Brownian motion, t denotes the time variable, $\sigma(t) = \sigma_{\min} \left(\frac{\sigma_{\max}}{\sigma_{\min}} \right)^t$, σ_{\min} and σ_{\max} are hyperparameters set to 0.01 and 50, respectively. During training, the score network $\Theta^h(\theta(t), t | \psi^{h'})$ learns the score equation $\nabla_{\theta} \log p_t(\theta(t) | \psi^{h'})$, where $p_t(\theta(t) | \psi^{h'})$ is the marginal distribution of $\theta(t)$ at time t . Based on Denoising Score Matching (DSM) (Vincent 2011), the loss function used to train the score network is

$$\mathcal{L}_{diff}^h = \sigma^2(t) \cdot \left\| \Theta^h(\theta(t), t | \psi^{h'}) - \frac{\theta(0) - \theta(t)}{\sigma^2(t)} \right\|_2^2, \quad (22)$$

where $t \sim \mathcal{U}(\epsilon, 1)$ with the hyperparameter $\epsilon \rightarrow 0$ set to 10^{-5} . During inference, we sample N pose candidates $\{\theta_i(t_f)\}_i^N$ from a Gaussian distribution $\mathcal{N}(\mathbf{0}, \sigma^2(t_f)\mathbf{I})$. For each sample $\theta_i(t_f)$, the final candidate $\theta_i(0)$ is obtained by solving the probability flow ODE (PF-ODE) (Song et al. 2021) from $t = t_f$ to $t = \epsilon$:

$$\frac{d\theta}{dt} = -\sigma(t)\dot{\sigma}(t)\nabla_\theta \log p_t(\theta|\psi^{h'}), \quad (23)$$

where t_f is a hyperparameter set to 0.55 for human hands and 0.65 for objects in our experiments. The PF-ODE is solved using the RK45 ODE solver (Dormand and Prince 1980).

As illustrated in Figure 9, the hand candidate generator network Θ^h takes as input 1) the hand feature $\psi^{h'}$, 2) the sampled pose $\theta(t) \in \mathbb{R}^{16 \times 6}$, and 3) the time variable t . The processing steps are as follows: 1) $\psi^{h'}$ is passed through two residual blocks, then reshaped into a feature vector $\psi^{h''}$. 2) $\theta(t)$ is processed through two fully connected layers, yielding the feature vector $\psi^\theta \in \mathbb{R}^{256}$. 3) t is encoded into a feature vector $\psi^t \in \mathbb{R}^{128}$ (Song et al. 2021). Then these three feature vectors, $\psi^{h''}$, ψ^t , and ψ^θ are concatenated and passed through multiple fully connected layers to predict the score of each joint $\{\frac{\partial S}{\partial \theta[j,:]} \}_{j=1}^{J^h}$, with $S = \log p_t(\theta(t)|\psi^h)$. In addition to skeletal 3D hand pose θ , the MANO hand model also contains the hand shape parameter vector $\beta \in \mathbb{R}^{10}$. It is predicted by a regression branch, consisting of three fully connected layers, that takes $\psi^{h''}$ as input and outputs the hand shape parameter β as well as the pose parameter θ_{reg} .

For object candidate generation, an object candidate generator Θ^o produces a set of plausible object poses $\{\phi_i\}_{i=1}^N$. Here $\phi_i \in \mathbb{R}^9$ contains the object pose parameters (R, T) , with $R \in \mathbb{R}^6$ representing the continuous 6D rotation parameters, and $T \in \mathbb{R}^3$ the translation parameters. The object candidate generator network follows a similar architecture but does not include a regression branch. Instead, it outputs gradient scores $\{\frac{\partial S}{\partial R}, \frac{\partial S}{\partial T}\}$ in the score prediction branch.

Implementation Details

Hyper-parameters Settings

The number of hand joints $|J^h|$ is set to 21, following the MANO model. The number of object keypoints $|K^o|$ is set to 27, consisting of one center point, eight corner points, twelve edge midpoints, and six face midpoints. The heatmap dimensions h_m and w_m are set to 64. The friction coefficient μ is set to 1.0. The number of base vectors N_v is set to 12. The loss weights are configured as follows: $\lambda_{hmap} = 10^3$, $\lambda_F = 10$, $\lambda_c = 10^2$, $\lambda_{force} = 1$, $\lambda_{torque} = 30$, $\lambda_\theta = 1$, $\lambda_\beta = 10$, and $\lambda_V = 10^4$. The candidate generator module produces 100 pose candidates for both the hand and the object. In visual-based aggregation, the top-K size is set to 30 for the hand and 5 for the object. In physics-based aggregation, the top-K size is 10 for both the hand and the object.

Training Details

The input images are cropped to (256, 256) pixels, and the batch size is set to 64. The data augmentation strategies in-

Method	Hand			Object		
	MJE	PA-MJE	MME	MCE	OCE	ADDS
Random	17.11	6.87	16.47	45.82	41.50	23.78
Baseline 1	12.26	5.32	11.90	35.88	32.57	28.37
Baseline 2	12.27	5.26	11.01	34.71	31.62	17.80
Baseline 3	12.69	5.56	12.21	30.01	25.53	14.94
VA	10.05	5.09	9.77	28.63	26.12	15.21
VA + PA	10.01	5.08	9.73	26.23	23.72	13.47

Table 7: Analysis of aggregation strategy on *DexYCB Full* (metrics, except CP, are in mm).

clude random rotation, translation, color jittering and Gaussian noise. The network parameters are optimized with the AdamW optimizer. The learning rate is initially set to 1e-4 and decays exponentially with an exponent of 0.98. The overall loss is formulated as $\mathcal{L} = \mathcal{L}_{hmap} + \mathcal{L}_{Phy} + \mathcal{L}_{pose}$. Typically, the overall loss converges after 45 epochs. During both training and testing phases, we determine to apply physical constraints or not, based on whether the hand is grasping the object and lifting it off the table. If the object is lifted more than 5 cm above the tabletop, apply the physical constraints for hand-object interaction; conversely, if the distance remains within 5 cm off the tabletop, we assume it is primarily supported by the table, thus do not apply the physical constraints. The experiments are conducted on a PC with two RTX 4090 GPUs.

Influence of Candidate Number and Top-K Size

We investigate the impact of the number of pose candidates and the Top-K selection sizes in both visual-based aggregation (VA) and physics-based aggregation (PA) on overall performance and computational complexity, as shown in Table 6. Increasing the number of candidates from 50 to 200 consistently improves both hand and object accuracy, with the mean joint error (MJE) decreasing from 10.12 to 10.00 and the object ADD-S improving from 14.03 to 12.89, albeit at the cost of increased GFLOPs. Notably, expanding the Top-K size in VA from 10 to 60 while keeping PA fixed degrades object performance (ADDS rises from 13.48 to 14.33), suggesting that overly large visual candidate pools may introduce noise. In contrast, adjusting the Top-K size in PA shows a marginal effect on performance, indicating that PA is relatively robust to this hyperparameter. Based on this analysis, a balanced configuration using 100 candidates, VA Top-K sizes of 30 for the hand and 10 for the object, and PA Top-K sizes of 5 for both hand and object achieves strong performance across both hand and object metrics, without incurring additional computational cost.

Analysis of Aggregation Strategy

The effectiveness of the proposed candidates aggregation strategy is compared with the following baselines: *Random* denotes to randomly select a candidate. *Baseline 1* denotes to average all candidates. *Baseline 2* denotes the highest

likelihood solution. *Baseline 3* denotes sorting based on the distance between the predicted 2D joints and the projected 2D joints of the candidates, and then averaging the top-K candidates with smaller average distances. *VA* denotes the visual cue-based aggregation strategy. *VA + PA* denotes the proposed aggregation strategy. The number of candidates is set to 100. The size of top-K is set to 30 for hand and 10 for object. *MME* denotes the mean mesh error.

Experimental results are shown in Table 7. *Random* directly uses a random candidate, which includes a lot of noises, leading the worst performance. *Baseline 1* and *Baseline 2* use simple aggregation strategies, significantly improving the hand-object pose estimation accuracy. It suggests that candidate aggregation is important for a multi-hypotheses method. *Baseline 3* attempts to incorporate visual cues by leveraging predicted 2D joint locations for candidate selection. However, it performs worse than *Baseline 1* and *Baseline 2* for hand estimation. This degradation is primarily due to frequent occlusions during hand-object interactions, which impair the reliability of 2D joint predictions. In contrast, our *visual-based* aggregation strategy leverages heatmaps as visual cues to progressively refine hand pose selection. This approach leads to substantial improvements in hand pose accuracy while maintaining comparable object estimation performance to *Baseline 3*. Finally, our full method (*Ours*) combines visual-based aggregation and physics-based aggregation. This strategy achieves the best overall performance across both hand and object metrics, demonstrating the complementary strengths of visual and physical reasoning in candidate aggregation.

Detailed Performance on *DexYCB Full* Dataset

We provide a detailed performance analysis of the hand pose accuracy on the *DexYCB Full* dataset, including separate evaluations for the left hand, right hand, and both hands, as well as per-joint accuracy. The results are summarized in Table 8. Additionally, Table 9 reports per-object performance on the *DexYCB Full* dataset. For object pose estimation, we also evaluate the following metrics: Average Distance of Model Points (ADD, mm); ADD with a threshold of 10% of the object’s diameter (ADD0.1d); average distance to the closest model point with a 10% diameter threshold (ADD0.1d); and Reprojection Error (REP, pixel).

Analysis of Inference Time

As shown in Table 10, the main computational bottleneck lies in the Candidate Generation stage, which relies on a score-based diffusion model to produce pose candidates. We acknowledge that diffusion-based models tend to have higher inference costs compared to deterministic regressors. However, our key contribution lies in the visual-physical representation learning and visual-physical aggregation framework, both of which are agnostic to the choice of candidate generator. This modular design allows our approach to seamlessly integrate with more efficient generators (e.g., VAE or flow-based models), which can substantially reduce inference time without altering the overall framework. We believe this flexibility enhances the practical scalability and general applicability of our method.

Metric	Joint Index	Right	Left	Both
MJE	1	3.89	4.11	4.00
MJE	2	6.71	6.92	6.82
MJE	3	8.88	9.14	9.01
MJE	4	12.28	12.73	12.50
MJE	5	7.51	7.67	7.59
MJE	6	9.33	9.78	9.55
MJE	7	10.72	11.20	10.96
MJE	8	13.16	14.08	13.61
MJE	9	7.72	8.04	7.88
MJE	10	10.01	10.28	10.15
MJE	11	11.72	11.79	11.76
MJE	12	15.12	14.95	15.04
MJE	13	7.37	7.74	7.55
MJE	14	9.77	9.92	9.84
MJE	15	12.14	11.88	12.01
MJE	16	16.26	15.48	15.88
MJE	17	7.62	8.09	7.85
MJE	18	9.73	10.26	9.99
MJE	19	11.96	12.31	12.14
MJE	20	16.11	15.99	16.05
MJE	all	9.91	10.11	10.01
PA-MJE	all	5.16	4.99	5.08

Table 8: Detailed hand pose accuracy on *DexYCB Full* dataset.

Object	MCE	OCE	ADD	ADDS	ADD _{0.1d}	ADDS _{0.1d}	REP
002_master_chef_can	20.74	19.74	43.06	10.31	34.12%	91.83%	21.44
003_cracker_box	23.99	22.64	25.04	12.00	72.18%	94.84%	8.02
004_sugar_box	24.54	21.81	28.76	12.12	59.03%	89.15%	10.18
005_tomato_soup_can	22.14	21.02	32.23	11.09	23.73%	80.85%	13.90
006_mustard_bottle	18.75	17.31	22.64	9.11	70.39%	94.44%	9.30
007_tuna_fish_can	21.66	20.98	35.59	11.16	15.82%	77.40%	17.03
008_pudding_box	37.98	36.28	43.38	25.44	52.82%	85.95%	183.34
009_gelatin_box	24.78	23.39	28.30	12.57	38.29%	78.09%	9.52
010_potted_meat_can	21.60	20.31	30.15	10.96	40.26%	83.32%	13.65
011_banana	28.61	23.04	34.98	13.75	48.11%	84.99%	14.08
019_pitcher_base	35.09	33.32	41.05	18.29	57.81%	91.82%	16.77
021_bleach_cleanser	26.70	22.72	32.74	12.65	64.30%	92.56%	14.67
024_bowl	21.00	19.80	65.25	11.22	22.24%	92.32%	36.71
025_mug	20.24	19.86	29.91	9.41	37.47%	91.21%	13.01
035_power_drill	29.88	28.18	32.34	14.73	58.98%	88.99%	11.57
036_wood_block	29.76	24.86	95.41	14.34	7.20%	88.93%	55.23
037_scissors	34.19	28.43	38.84	17.82	34.48%	75.57%	14.56
040_large_marker	25.39	22.20	29.06	14.65	10.52%	67.41%	11.33
052_extra_large_clamp	33.74	26.21	56.29	15.64	29.09%	87.04%	27.86
061_foam_brick	23.32	21.67	44.41	11.73	11.31%	72.20%	22.06
average_instance	26.23	23.72	39.20	13.47	39.65%	85.46%	26.40

Table 9: Per-object performance on *DexYCB Full* dataset.

Module	Time (ms)
Feature extraction	18.6
Candidate Generation (hand)	34.5
Candidate Generation (object)	25.6
Visual-based aggregation (hand)	18.9
Visual-based aggregation (object)	6.75
Physics-based aggregation (hand)	10.6
Physics-based aggregation (object)	4.1
Total	119.05

Table 10: Runtime analysis of each module in our framework.